

Few Shot Alternating GD and Minimization for Generalizable Real-Time MRI

Silpa Babu, *Member, IEEE*, Sajan Goud Lingala, *Member, IEEE*, and Namrata Vaswani, *Fellow, IEEE*

Abstract—This work introduces a novel “near” real-time (real-time after an initial short delay) MRI solution that handles motion well and is generalizable. Here, real-time means the algorithm works well on a highly accelerated scan, is zero-latency (reconstructs a new frame as soon as MRI data for it arrives), and is fast enough, i.e., the time taken to process a frame is comparable to the scan time per frame or lesser. We demonstrate its generalizability through experiments on 6 prospective datasets and 17 retrospective datasets that span multiple different applications, sampling schemes, and rates. Comparisons with a large number of existing real-time and batch methods, including unsupervised and supervised deep learning methods, show the power and speed of our approach.

Index Terms—real-time, generalization, dynamic MRI

I. INTRODUCTION

Magnetic Resonance Imaging (MRI) is a safe modality for non-invasive dynamic imaging of human organ cross-sections (slices). MRI scans, after some pre-processing, can be interpreted as 2D Fourier transform (FT) coefficients of the organ slice of interest. These are acquired sequentially one row, or radial spoke, of coefficients at a time, making the scanning slow. The scan can be accelerated by undersampling the FT according to a pre-specified trajectory, and using various modeling assumptions to still obtain an accurate reconstruction. For use in interventional radiology (interactive) applications such as real-time ungated free breathing cardiac MRI or visualizing articulatory movements in biofeedback type experiments, there is a need to obtain real-time reconstructions.

A. Existing Work

Accelerated dynamic MRI algorithms have been extensively studied. Broadly speaking there are a few classes of recent approaches – sparsity (compressed sensing) based methods, e.g., [2] and follow-up works, low-rank (LR), including LR+S, based methods [3], [4], [5], [6], [7] and many others, supervised deep learning (DL) methods, e.g., [8], more recent unsupervised DL methods [9], [10], [11], and real-time MRI solutions [12], [13], [14], [15], [16], [17], [18]. Supervised DL methods require a lot of training data which is not easy to obtain for dynamic imaging (except for a few settings such as breath-held cardiac) and hence are unusable for most

applications. Unsupervised DL methods do not require training data, making them usable for new datasets (in principle). However, in practice, as we demonstrate, without architecture or parameter tuning, these also do not work well for unseen data. Additionally, they are very slow/expensive at inference time since the DL model is both learning parameters and inferring using the input k-space dataset. For the same reason, these cannot be used to get a real-time solution.

Real-time approaches [12], [13], [14], [16], [17], [15] are more generalizable than DL methods, but do not work well for datasets with significant motion. The reason is most of these methods combine the scan data from multiple consecutive frames, or use the high spatial frequency information from just the first (reference) frame.

Overall LR-based (including LR+S) methods are the most generalizable since these are able to handle motion well, and do not have too many tuning parameters or model type choices. For example, a sparsifying dictionary/basis or model architecture does not need to be chosen. However, most of these methods are slow and/or memory-intensive.

We modify the linear few shot learning (FSL) idea from recent works [19], [20], [21] to modify the approach of [7]. Linear FSL learns the model parameters for a new linear regression task using highly undersampled data for that task. The assumption is that this task is similar to an existing set of α similar tasks for which a common “representation” can be learned. In the linear case, the similarity is modeled by assuming that the matrix formed by the model parameter vectors for these tasks is LR. In existing literature [22], FSL is only used for DL methods and means something completely different there.

B. Contributions

(1) This work introduces a novel “near real-time” MRI solution, dynamic few shot MRI (FS-MRI), that handles motion well and is generalizable: the same algorithm, without any parameter tuning, achieves highly accurate reconstructions across various MRI applications, sampling patterns, and rates. Moreover, our algorithm also provides a delayed set of reconstructions that are of improved quality. Generalizability is needed for an algorithm to be practically usable on an MRI scanner. Real-time means the algorithm works well on a highly accelerated (undersampled) scan; is zero-latency (reconstructs a new frame as soon as k-space data for it arrives); and is fast enough – the time taken to process a frame is comparable to the scan time per frame or lesser. Near real-time means it is real-time after an initial short delay of α frames. (2) We explain how we can develop a distributed version of FS-MRI

This work was supported by NSF under Grant CCF-2341359 and NIH under Grant R01-HL173483. A part of this work will appear in ICASSP 2025 [1], this short version does not do an exhaustive comparison of various methods and almost no prospective ones.

Silpa Babu and Namrata Vaswani are with the Department of Electrical and Computer Engineering, Iowa State University, USA (e-mail: sbabu@iastate.edu; namrata@iastate.edu). Sajan Goud Lingala is with the Department of Biomedical Engineering, University of Iowa, USA (e-mail: sajangoud-lingala@uiowa.edu).

	FS-MRI (proposed)	LR methods	DL Unsupervised	DL Supervised	Existing Real-time Techniques
Accuracy	Best	Good	Bad	Bad	Bad
Inference Compute Time	Low	Low	High	High	Lowest
Real-Time	Yes (nearly)	No	No	No	Yes
Memory Req.	Lowest	Low	High	High	Lowest
Needs Training Data	No	No	No	Yes	No
Average Time per Frame (Python)	0.0385	-	0.3613	0.1735	-
(MATLAB)	0.1069	0.1518	-	-	0.0028

TABLE I: Overall comparison for generalizability (accuracy across various applications, sampling schmes and rates) for various classes of algorithms. This table summarizes information from Tables IIa and IIb given later.

to speed it up further. (3) We develop its view-sharing based modification to handle highly undersampled spiral datasets.

(4) We demonstrate the generalizability of FS-MRI through experiments on 6 prospective datasets and 17 retrospective multi-coil k-space datasets that span multiple different applications – speech larynx imaging, brain, ungated cardiac perfusion, cardiac cine, free breathing cardiac OCMR, abdomen; sampling schemes – Cartesian, pseudo-radial, radial, spiral; and sampling rates (as low as 4 radial lines per frame). Our work also provides an exhaustive comparison of our algorithms (FS-MRI and VS-FS-MRI) with state-of-the-art (SOTA) approaches from various classes of accelerated dynamic MRI solutions - one SOTA supervised DL method, CineVN [8]; three SOTA unsupervised DL methods - varMRI [9] and two versions of DEBLUR [10]; a few of the most well-known real-time dynamic MRI solutions – keyhole imaging, view sharing, and OnAIR [12], [13], [15], [17]; and three of the best known LR, including L+S, solutions (all batch methods) – kt-SLR, L+S-Otazo, L+S-Lin, and altGDmin-MRI [4], [5], [6], [7]. Each algorithm is compared on all the above stated datasets, without any parameter tuning. We show that FS-MRI algorithm has the lowest or second lowest reconstruction error for all retrospective datasets, and has excellent visual quality on almost all of them. It is also faster than all algorithms except the real-time ones, but these have poor reconstruction quality for datasets with motion. Our overall conclusions are summarized in Table I above.

FS-MRI assumes a slow-changing hierarchical 3-level LR model with the third level being full rank (used to model changing details). It uses this to develop a novel dynamic linear FSL algorithm that modifies the batch alternating GD and minimization (altGDmin) based method from [7]. In [7], we introduced a batch solution for LR-then-S (LR followed by temporal sparse) accelerated dynamic MRI. The algorithm needed to wait for the entire sequence to be acquired before reconstruction could begin. Sparsity was imposed in the last step and along the temporal axis, preventing the design of a real-time modification. It did briefly introduce a different online method, but that method could not handle motion well and hence did not generalize. In contrast, FS-MRI is near real-time and generalizable, and much faster. For long sequences such as the speech sequence, for 16 radial lines setting, FS-MRI is 1.4 times faster than the approach of [7], while having equally good or better accuracy. FS-MRI Python GPU implementation is 2.5 times faster. Accuracy is often better because our new slow changing model is a better one. See the caption of Fig 2 and Table IIb.

C. Problem setting

1) *Goal*: Our goal is generalizable and near real-time MRI. An initial mini-batch of α frames are processed as a batch, but, after this, the algorithm operates in real-time. The goal in real-time imaging is three-fold. We need the algorithm to work with highly-undersampled scans (fast scan time); we need it to be online/zero-latency, i.e., to recover the k -th image z_k^* , as soon as the k-space data (Fourier measurements) for it, y_k , arrive; and we need it to be fast, the per-frame reconstruction time should be equal to or lower than the per-frame scan time. We also need generalizability.

2) *Cartesian MRI measurement model*: To explain the model simply, we assume that the unknown MRI images are vectorized and arranged as columns of an $n \times q$ matrix, $\mathbf{Z}^* = [z_1^*, z_2^*, \dots, z_q^*]$; thus z_k^* is the k -th image of the sequence vectorized. Let \mathbf{F} be an $n \times n$ matrix that models the 2D discrete Fourier Transform (DFT) operation on the vectorized image; thus $\mathbf{F}z$ is the vectorized 2D-DFT of vectorized image z . A broad 1-0 matrix \mathbf{H}_k of size $m_k \times n$ models the undersampling operation: each row of it contains exactly one 1 corresponding to the DFT coefficient that is observed. Thus \mathbf{H}_k specifies the sampling mask. Let $\mathbf{A}_k = \mathbf{H}_k \mathbf{F}$. In single-coil Cartesian MRI, one needs to recover the images z_k^* from measurements $y_k := \mathbf{A}_k z_k^* = (\mathbf{H}_k \mathbf{F}) z_k^*$, $k \in [q]$.

In case of multi-coil Cartesian MRI, there are multiple receive channels (coils), each measuring a subset of Fourier coefficients of a differently weighted version of the cross-section to be imaged. Denote the number of coils by c . Let $y_{k,j}$ denote the measurements at the j -th coil. Then, $y_k^\top = [y_{k,1}^\top, y_{k,2}^\top, \dots, y_{k,c}^\top]$ and $y_{k,j} = \mathbf{H}_k \mathbf{F} \mathbf{D}_j z_k^*$, where $\mathbf{D}_j = \text{diag}(\mathbf{d}_j, j = 1, 2, \dots, n)$ are $n \times n$ diagonal matrices with diagonal entries (entries of the vector \mathbf{d}_j) being the coil sensitivities of the j -th coil.

Let $m = \max_k(m_k)$. We define the $mc \times n$ matrix $\mathbf{Y} = [(y_1)_{\text{long}}, (y_2)_{\text{long}}, \dots, (y_q)_{\text{long}}]$ with $(y_k)_{\text{long}}$ being the vector y_k followed by $(m - m_k)c$ zeros. Similarly let $(\mathbf{A}_k)_{\text{long}}$ be an $mc \times n$ matrix with $(m - m_k)c$ rows of zeros at the end. Then, the above model can also be expressed as $\mathbf{Y} = \mathcal{A}(\mathbf{Z}^*) = [(\mathbf{A}_1)_{\text{long}}(z_1^*), (\mathbf{A}_2)_{\text{long}}(z_2^*), \dots, (\mathbf{A}_q)_{\text{long}}(z_q^*)]$.

3) *Radial MRI*: The above matrix-vector model is valid when the samples are available on a Cartesian grid; either they are acquired that way or they are mapped onto a Cartesian grid, e.g., in case of pseudo-radial sampling. When directly using true radial samples, the main ideas above, and in our algorithms given below, are still exactly the same, except that the DFT gets replaced by non-uniform FT (NUFT), e.g., [23].

II. FEW SHOT ALTGDMin FOR REAL-TIME MRI

A. Proposed slow-changing 3-level LR model

We introduce the following slow-changing hierarchical 3-level LR model on the image sequence. Split the q -frame sequence into q/α mini-batches, each of size α frames. Assume here that q/α is an integer. Define the mini-batches, $\mathcal{S}_\ell := [(\ell - 1)\alpha + 1, \ell\alpha]$ and let $\mathbf{Z}^*_{(\ell)} := [\mathbf{z}^*_k, k \in \mathcal{S}_\ell]$. We assume that (1) each image within the mini-batch is a sum of three layers – a common (rank $r = 1$) component; a LR (rank r) component that models the fact that image changes over time depend on a much smaller number, r , of factors than the sequence length α ; and a full-rank (rank $\min(n, \alpha)$) component with no temporal dependencies. Also, (2) the magnitude of each layer is much smaller than that of the previous layer. (3) Over consecutive mini-batches, the “mean” image changes slowly; and the same is true for the column-span of the LR component. This last assumption is the one that helps us obtain a near real-time algorithm.

To define the model mathematically, we need some notation. Let $\mathbf{1}$ denote a vector of α ones; for two $n \times r$ matrices with orthonormal columns, $\mathbf{U}_1, \mathbf{U}_2$, $\text{SD}(\mathbf{U}_1, \mathbf{U}_2) := \|(\mathbf{I} - \mathbf{U}_1\mathbf{U}_1^\top)\mathbf{U}_2\|_F$ denotes the Subspace Distance (SD) between the subspaces spanned by their columns; $\|\cdot\|$ denotes the (induced) l_2 norm of a vector/matrix and $\|\cdot\|_F$ denotes matrix Frobenius norm. The SD between two r -dimensional subspaces is a real number between 0 and \sqrt{r} . Then, for all $\ell = 1, 2, \dots, q/\alpha$,

$$\begin{aligned} \mathbf{Z}^*_{(\ell)} &:= \bar{\mathbf{z}}^*_{(\ell)}\mathbf{1}^\top + \mathbf{U}^*_{(\ell)}\mathbf{B}^*_{(\ell)} + \mathbf{E}^*_{(\ell)}, \\ \|\mathbf{E}^*_{(\ell)}\|_F &\ll \|\mathbf{B}^*_{(\ell)}\|_F \ll \|\bar{\mathbf{z}}^*_{(\ell)}\|_F\sqrt{\alpha}, \\ \|\bar{\mathbf{z}}^*_{(\ell)} - \bar{\mathbf{z}}^*_{(\ell-1)}\| &\ll \|\bar{\mathbf{z}}^*_{(\ell-1)}\|, \\ \text{SD}(\mathbf{U}^*_{(\ell)}, \mathbf{U}^*_{(\ell-1)}) &\ll \sqrt{r} \end{aligned} \quad (1)$$

with $\bar{\mathbf{z}}^*_{(0)} = \mathbf{0}_n$ and $\mathbf{U}^*_{(0)} = \mathbf{0}_{n \times r}$. In the above model, $\bar{\mathbf{z}}^* \in \mathbb{R}^n$ is the common “mean image” component for the entire mini-batch, $\mathbf{U}^* \in \mathbb{R}^{n \times r}$ is a matrix with orthonormal columns whose span equals the column-span of the LR component, $\mathbf{B}^* = [\mathbf{b}^*_k, k \in \mathcal{S}_\ell] \in \mathbb{R}^{r \times \alpha}$ with each \mathbf{b}^*_k being an r length vector, and $\mathbf{E}^* = [\mathbf{e}^*_k, k \in \mathcal{S}_\ell] \in \mathbb{R}^{n \times \alpha}$ is the full-rank component with no model assumed. This models the finer details that are different in each image.

B. AltGDmin (AGM) and practical AGM [24], [25]

AltGDmin is a fast GD based algorithm to recover a rank- r $n \times q$ matrix \mathbf{X} factored as $\mathbf{X} = \mathbf{U}\mathbf{B}$ where \mathbf{U} is an $n \times r$ matrix with orthonormal columns and \mathbf{B} is an $r \times q$ matrix by minimizing $f(\mathbf{U}, \mathbf{B}) := \sum_{k=1}^q \|\mathbf{y}_k - \mathbf{U}\mathbf{b}_k\|_2^2$. It was introduced and analyzed, and evaluated for MRI data in our past works [24], [25].

1) *AltGDMin (AGM) Input and Output*: The algorithm input consists of MRI scan data \mathbf{y}_k , the scan trajectory matrices \mathbf{H}_k and hence $\mathbf{A}_k = \mathbf{H}_k\mathbf{F}$, $k \in [q]$, and an initialization for \mathbf{U} , denoted \mathbf{U}_{init} . When the initialization is not provided, it can be computed using the spectral initialization method described below with $\mathbf{y}_k, \mathbf{A}_k, k \in [q]$ as input. The output of AGM is a final estimate of \mathbf{U}, \mathbf{B} , and hence of $\mathbf{X} = \mathbf{U}\mathbf{B}$.

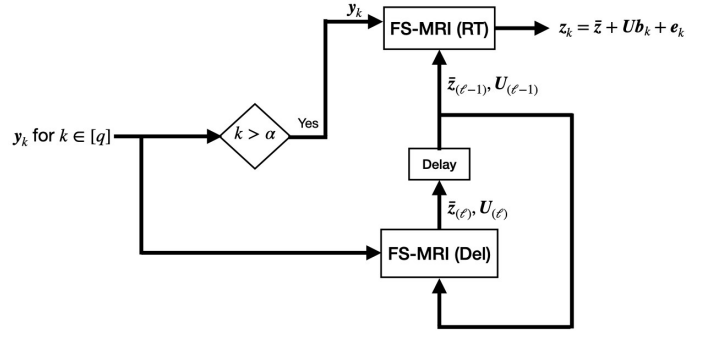


Fig. 1: This figure shows how the real-time (RT) and mini-batch (delayed) components of FS-MRI interact with each other.

2) *AGM main idea*: Given an initialization \mathbf{U}_{init} , AGM starts with $\mathbf{U} = \mathbf{U}_{\text{init}}$ and alternates between the following two steps: (1) For each new estimate of \mathbf{U} , we solve for \mathbf{B} by minimizing $f(\mathbf{U}, \mathbf{B})$ over it, while keeping \mathbf{U} fixed at its current value. Because our measurements are column-wise decoupled, this step gets decoupled for the different columns of \mathbf{B} , and simplifies to solving q different r -dimensional least squares (LS) problems

$$\arg \min_{\mathbf{b}_k} \|\tilde{\mathbf{y}}_k - \mathbf{A}_k \mathbf{U} \mathbf{b}_k\|^2 = (\mathbf{A}_k \mathbf{U})^\dagger \mathbf{y}_k, \quad k \in [q]$$

where $\mathbf{M}^\dagger := (\mathbf{M}^\top \mathbf{M})^{-1} \mathbf{M}^\top$. (2) We update \mathbf{U} using a single GD step followed by orthonormalizing its output using QR decomposition: $\mathbf{U}^+ = \text{QR}(\mathbf{U} - \eta \nabla_{\mathbf{U}} f(\mathbf{U}, \mathbf{B}))$. For our cost function, $\nabla_{\mathbf{U}} f(\mathbf{U}, \mathbf{B}) = \sum_k \mathbf{A}_k^\top (\mathbf{y}_k - \mathbf{A}_k \mathbf{U} \mathbf{b}_k) \mathbf{b}_k^\top$. Here η is the GD step-size (learning rate).

3) *Spectral initialization*: Given inputs $\mathbf{y}_k, \mathbf{A}_k, k \in [q]$, we first compute a truncation threshold $\gamma = 9 \frac{1}{mq} \sum_{ki} |\mathbf{y}_{ki}|^2$ to discard outliers. We then compute $\mathbf{y}_{k, \text{trunc}} = \mathbf{y}_k \circ \mathbb{1}\{|\mathbf{y}_k| \leq \sqrt{\gamma}\}$ and use this, and $\bar{m} = \sum_{k=1}^q m_k/q$, to obtain the initialization matrix \mathbf{X}_0 as:

$$\mathbf{X}_0 = \left[\frac{1}{\sqrt{m_1 \bar{m}}} (\mathbf{A}_1^\top \mathbf{y}_{1, \text{trunc}}), \dots, \frac{1}{\sqrt{m_q \bar{m}}} (\mathbf{A}_q^\top \mathbf{y}_{q, \text{trunc}}) \right] \quad (2)$$

In the above \circ denotes the Hadamard product (\cdot operation in MATLAB). Compute \mathbf{U}_{init} as the top r left singular vectors \mathbf{X}_0 with

$$r = \min\{\hat{r} : \sum_{j=1}^{\hat{r}} \sigma_j^2(\mathbf{X}_0) \geq 0.85 \sum_{j=1}^{r_{\text{big}}} \sigma_j^2(\mathbf{X}_0)\} \quad (3)$$

where $r_{\text{big}} = \min(n, q, \min_k m_k)/10$ and σ_j is the j -th singular value of \mathbf{X}_0 .

4) *Parameter setting*: We set r as above. We set $\eta = 0.14 / \|\nabla_{\mathbf{U}} f(\mathbf{U}_{\text{init}}, \mathbf{B}_{\text{init}})\|$ with \mathbf{B}_{init} being an $r \times q$ matrix with k -th column $\mathbf{b}_k = (\mathbf{A}_k \mathbf{U}_{\text{init}})^\dagger \mathbf{y}_k$. We run our algorithm for at most T_{max} iterations, but allow it to exit sooner if the estimates do not change much: if $\text{SD}(\mathbf{U}^+, \mathbf{U}) \leq 0.01\sqrt{r}$.

C. Proposed algorithm: Dynamic Few Shot MRI

We develop dynamic few shot MRI using altGDmin (AGM) as follows.

Algorithm 1 *FewShot-MRI: real-time component.*

```

1: Input:  $\mathbf{y}_k, \mathbf{A}_k$ 
2:  $\ell \leftarrow \lceil \frac{k}{\alpha} \rceil + 1$ 
3: Get  $\mathbf{U} \leftarrow \mathbf{U}_{(\ell-1)}$  and  $\bar{\mathbf{z}} \leftarrow \bar{\mathbf{z}}_{(\ell-1)}$  from Algorithm 2.
4:  $\tilde{\mathbf{y}}_k \leftarrow \mathbf{y}_k - \mathbf{A}_k \bar{\mathbf{z}}$ 
5:  $\mathbf{b}_k \leftarrow (\mathbf{A}_k \mathbf{U})^\dagger \tilde{\mathbf{y}}_k$ 
6:  $\mathbf{e}_k \leftarrow \text{CGLS}(\tilde{\mathbf{y}}_k - \mathbf{A}_k \mathbf{U} \mathbf{b}_k, \mathbf{A}_k, \mathbf{0}, 3)$ 
7: Output:  $\mathbf{z}_k = \bar{\mathbf{z}} + \mathbf{U} \mathbf{b}_k + \mathbf{e}_k$ 

```

1) *Initial mini-batch computation:* We wait for the under-sampled k-space data of the first mini-batch of α frames, $\mathbf{y}_k, k \in \mathcal{S}_1$. We use this to first estimate $\bar{\mathbf{z}}_{(1)}$ as follows. Using the fact that the other two components, $\mathbf{U}^* \mathbf{B}^*, \mathbf{E}^*$, are much smaller in magnitude, we can find $\bar{\mathbf{z}}$ by solving $\arg \min_{\bar{\mathbf{z}}} \sum_{k \in [\alpha]} \|\mathbf{y}_k - \mathbf{A}_k \bar{\mathbf{z}}\|_2^2$. While this is a LS problem with a closed form solution, computing it is very memory-intensive since it requires inverting an $n \times n$ matrix where n is the number of pixels in one image. Hence we use the conjugate gradient LS (CGLS) sub-routine from MATLAB or Python. Let $\mathbf{y}_{(1)} = [\mathbf{y}_k^\top, k \in \mathcal{S}_1]^\top$ and $\mathbf{A}_{(1)} = [\mathbf{A}_k^\top, k \in \mathcal{S}_1]^\top$. We call it as $\text{CGLS}(\mathbf{y}_{(1)}, \mathbf{A}_{(1)}, \mathbf{z}_{\text{init}} = \mathbf{0}, \text{max-iter} = 10)$. Next, we compute the residual measurements, $\tilde{\mathbf{y}}_k = \mathbf{y}_k - \mathbf{A}_k \bar{\mathbf{z}}_{(1)}, k \in \mathcal{S}_1$. These and \mathbf{A}_k are first used to compute the rank r and the spectral initialization \mathbf{U}_{init} as explained in Sec. II-B3. We then call the AGM sub-routine as $\text{AGM}(\{\tilde{\mathbf{y}}_k, \mathbf{A}_k, k \in \mathcal{S}_1\}, \mathbf{U}_{\text{init}}, T_{\text{max}} = 50)$. Its output is the final estimate of $\mathbf{U}_{(1)}$.

2) *Real-time algorithm:* Starting at time $k = \alpha + 1$, we use the slow mean change and slow subspace change assumptions to obtain real-time estimates as follows.

For times $k \in \mathcal{S}_\ell$, set $\bar{\mathbf{z}} = \bar{\mathbf{z}}_{(\ell-1)}$ and $\mathbf{U} = \mathbf{U}_{(\ell-1)}$. For $\ell = 2$, we obtain these from the initialization explained above. For $\ell > 2$, these are updated as explained below. Compute $\tilde{\mathbf{y}}_k = (\mathbf{y}_k - \mathbf{A}_k \bar{\mathbf{z}})$ and use this to obtain

$$\mathbf{b}_k = (\mathbf{A}_k \mathbf{U})^\dagger \tilde{\mathbf{y}}_k,$$

and

$$\mathbf{e}_k = \arg \min_{\mathbf{e}} \|(\tilde{\mathbf{y}}_k - \mathbf{A}_k \mathbf{U} \mathbf{b}_k) - \mathbf{A}_k \mathbf{e}\|^2 \text{ s.t. } \|\mathbf{e}\|^2 \leq \lambda$$

In the above, the constraint enforces the assumption that \mathbf{e}_k has small magnitude. In practice, this can be approximately solved quickly by starting with a zero initialization and using only a few CGLS iterations for the unconstrained problem. Thus, we obtain $\mathbf{e}_k = \text{CGLS}(\tilde{\mathbf{y}}_k - \mathbf{A}_k \mathbf{U} \mathbf{b}_k, \mathbf{A}_k, \text{init} = \mathbf{0}, \text{max-iter} = 3)$. Finally, output the real-time estimate

$$\mathbf{z}_k = \bar{\mathbf{z}} + \mathbf{U} \mathbf{b}_k + \mathbf{e}_k$$

3) *Mini-batch updates of the initial estimates of $\bar{\mathbf{z}}, \mathbf{U}$:*

If we have limited computational power, we would compute $\bar{\mathbf{z}}, \mathbf{U}$ only once using the first mini-batch. However, for image sequences with significant motion, this does not work well [7]. The reason is both $\bar{\mathbf{z}}$ and \mathbf{U} do change over time, albeit slowly. Instead, a better idea is to also update $\bar{\mathbf{z}}, \mathbf{U}$ every α frames in a mini-batch fashion, using the slowly changing assumption. This assumption makes the updating quick while keeping the algorithm accuracy comparable or better than that of a batch method. The accuracy is often better because slow changing

Algorithm 2 *FewShot-MRI: mini-batch component*

```

1: for  $\ell = 1$  to  $q/\alpha$  do
2:   Input:  $\mathbf{y}_k, \mathbf{A}_k, k \in \mathcal{S}_\ell$ 
3:    $\mathbf{y}_{(\ell)} = [\mathbf{y}_k^\top, k \in \mathcal{S}_\ell]^\top, \mathbf{A}_{(\ell)} = [\mathbf{A}_k^\top, k \in \mathcal{S}_\ell]^\top$ .
4:   if  $\ell = 1$  then
5:     % Initialization
6:      $\bar{\mathbf{z}} \leftarrow \text{CGLS}(\mathbf{y}_{(1)}, \mathbf{A}_{(1)}, \mathbf{0}, 10)$ 
7:      $\tilde{\mathbf{y}}_k \leftarrow \mathbf{y}_k - \mathbf{A}_k \bar{\mathbf{z}}$ , for all  $k \in [\alpha]$ .
8:     Compute  $r$  as explained in Sec. II-B3
9:     Compute  $\mathbf{U}_{\text{init}}$  as explained in Sec. II-B3.
10:     $[\mathbf{U}, \mathbf{B}] \leftarrow \text{AGM}(\{\tilde{\mathbf{y}}_k, \mathbf{A}_k, k \in \mathcal{S}_1\}, \mathbf{U}_{\text{init}}, 50)$ 
11:  else
12:    % Mini-batch update
13:     $\bar{\mathbf{z}} \leftarrow \text{CGLS}(\mathbf{y}_{(\ell)}, \mathbf{A}_{(\ell)}, \bar{\mathbf{z}}_{(\ell-1)}, 2)$ 
14:     $\tilde{\mathbf{y}}_k \leftarrow \mathbf{y}_k - \mathbf{A}_k \bar{\mathbf{z}}$ , for all  $k \in \mathcal{S}_\ell$ .
15:     $[\mathbf{U}, \mathbf{B}] \leftarrow \text{AGM}(\{\tilde{\mathbf{y}}_k, \mathbf{A}_k, k \in \mathcal{S}_\ell\}, \mathbf{U}_{(\ell-1)}, 15)$ 
16:  end if
17:   $\mathbf{e}_k \leftarrow \text{CGLS}(\tilde{\mathbf{y}}_k - \mathbf{A}_k \mathbf{U} \mathbf{b}_k, \mathbf{A}_k, \mathbf{0}, 3)$  for all  $k \in \mathcal{S}_\ell$ 
18:  Output:  $\bar{\mathbf{z}}_{(\ell)} \leftarrow \bar{\mathbf{z}}, \mathbf{U}_{(\ell)} \leftarrow \mathbf{U}$ 
19:  Output: Delayed recons  $\mathbf{z}_k = \bar{\mathbf{z}} + \mathbf{U} \mathbf{b}_k + \mathbf{e}_k, k \in \mathcal{S}_\ell$ 
20: end for

```

```

1: function  $\text{AGM}(\mathbf{y}_k, \mathbf{A}_k, k \in [q], \mathbf{U}_{\text{init}}, T_{\text{max}})$ 
2:    $\mathbf{U} \leftarrow \mathbf{U}_{\text{init}}$ 
3:   for  $t = 1$  to  $T_{\text{max}}$  do
4:      $\mathbf{b}_k \leftarrow (\mathbf{A}_k \mathbf{U})^\dagger \mathbf{y}_k$  for all  $k \in \mathcal{S}$ 
5:      $\nabla_U f(\mathbf{U}, \mathbf{B}) \leftarrow \sum_{k \in \mathcal{S}} \mathbf{A}_k^\top (\mathbf{A}_k \mathbf{U} \mathbf{b}_k - \mathbf{y}_k) \mathbf{b}_k^\top$ 
6:     If  $t = 1$ , set  $\eta = 0.14 / \|\nabla_U f(\mathbf{U}, \mathbf{B})\|$ .
7:      $\hat{\mathbf{U}}^+ \leftarrow \mathbf{U} - \eta \nabla_U f(\mathbf{U}, \mathbf{B}); \hat{\mathbf{U}}^+ \stackrel{\text{QR}}{\leftarrow} \mathbf{U} + \mathbf{R}^+$ .
8:     EXIT loop if  $\text{SD}(\mathbf{U}, \hat{\mathbf{U}}^+) / \sqrt{r} < \epsilon_{\text{exit}} = 0.01$ .
9:     Set  $\mathbf{U} \leftarrow \hat{\mathbf{U}}^+$ 
10:  end for
11:  return  $\mathbf{U}, \mathbf{B}$  with  $\mathbf{B} = [\mathbf{b}_1, \mathbf{b}_2, \dots, \mathbf{b}_q]$ 
12: end function

```

```

1: function  $\text{CGLS}(\mathbf{y}_k, \mathbf{A}_k, \mathbf{w}_{\text{init}}, \text{max-iter})$ 
2:    $\mathbf{w} \leftarrow \text{CGLS}(\mathbf{y}_k, \mathbf{A}_k, \mathbf{w}_{\text{init}}, \text{max-iter})$ 
3:   % (function in MATLAB and Python)
4:   return  $\mathbf{w}$ 
5: end function

```

model is a better one than a fixed subspace model. Slow $\bar{\mathbf{z}}$ change means that we now need to solve

$$\arg \min_{\bar{\mathbf{z}}} \sum_{k \in \mathcal{S}_\ell} \|\mathbf{y}_k - \mathbf{A}_k \bar{\mathbf{z}}\|_2^2 \text{ s.t. } \|\bar{\mathbf{z}} - \bar{\mathbf{z}}_{(\ell-1)}\|^2 \leq \lambda$$

We can get a quick approximate solution for this by using CGLS for the unconstrained problem with using the previous $\bar{\mathbf{z}}$ as the initialization, and using only 2 iterations instead of 10, i.e., use $\text{CGLS}(\mathbf{y}_{(\ell)}, \mathbf{A}_{(\ell)}, \bar{\mathbf{z}}_{(\ell-1)}, \text{max-iter} = 2)$ with $\mathbf{y}_{(\ell)} = [\mathbf{y}_k^\top, k \in \mathcal{S}_\ell]^\top$ and $\mathbf{A}_{(\ell)} = [\mathbf{A}_k^\top, k \in \mathcal{S}_\ell]^\top$. Slow subspace change means that we do not need the time-consuming spectral initialization step, and that we can use much fewer AGM iterations. We use $\text{AGM}(\{\tilde{\mathbf{y}}_k, \mathbf{A}_k, k \in \mathcal{S}_\ell\}, \mathbf{U}_{(\ell-1)}, T_{\text{max}} = 15)$. Here $\tilde{\mathbf{y}}_k = \mathbf{y}_k - \mathbf{A}_k \bar{\mathbf{z}}_{(\ell)}$. Use its output as the final $\mathbf{U}_{(\ell)}$.

This algorithm for updating $\bar{\mathbf{z}}$ and \mathbf{U} is also computing \mathbf{B} . By also adding one more quick step that updates \mathbf{e}_k , it gives us an improved delayed reconstruction of the image sequence.

We summarize these algorithms in Algorithms 1 and 2. Fig 1 shows how the two algorithms interact. Our method can be

interpreted as Dynamic Few Shot Learning. The mini-batch updates help dynamically update the linear representations, \bar{z} and U (really its column span), every so often, while the real-time component uses these for few shot learning of the images. Here the images are the model parameters.

D. Parallel Distributed FS-MRI

1) *Implementation Considerations*: In implementation, all of the above is implemented efficiently, and without using matrix-vector multiplies. Specifically, H_k (MRI trajectory) is implemented using undersampling, $D_j z$ is implemented using Hadamard product as $d_j \circ z$; and the FT is implemented using the 2D fast Fourier transform function (fft2) or fast NUFT (NUFFT) of [23]. Also, $A_k U$ for all k is implemented efficiently by first computing FU (FT of each of the r columns of U) and then using appropriate undersampling.

2) *Parallel Distributed FS-MRI*: Because of the simple nature of our algorithm (most operations within each iteration do not involve a loop), it can be easily distributed onto multiple cores of a CPU or GPU to enable faster computation. Our Python implementation does this automatically. We explain the ideas using single-coil MRI, but the extension to multi-coil is direct. Consider the AGM algorithm applied on the \tilde{y}_k s. At each iteration, we first compute (FU) (fft2 of its r columns). Next, the LS step involves computing $b_k = (H_k(FU))^\dagger \tilde{y}_k$ for all $k \in \mathcal{S}$. This can be distributed onto L cores with each core doing α/L of these computations. The gradient computation step requires computing $\sum_{k \in \mathcal{S}} F^\top (H_k^\top H_k(FU)b_k - H_k^\top y_k) b_k^\top$. For this we first compute (FU) B . The first expensive step is the computation of the inverse-fft2 of α different n -length vectorized images $w_k := H_k^\top H_k(FU b_k) - H_k^\top y_k$, $k \in \mathcal{S}$. This gets distributed onto L cores, each computing α/L of the inverse ffts. The last step of computing the α outer products $(Fw_k) b_k^\top$ is also similarly parallelized. The expensive step in learning or updating \bar{z} is the computation of the gradient in each iteration $\sum_{k \in \mathcal{S}} F^\top (H_k^\top H_k(F\bar{z}) - H_k^\top y_k) b_k^\top$. This can be also parallelized in a similar fashion as well.

E. View Sharing based modified FS-MRI

As explained earlier, view-sharing [15] is widely used to enhance temporal resolution in dynamic MRI by combining phase-encoding lines from multiple frames. However, motion and missing k-space samples can introduce artifacts. To address these issues, we propose VS-FS-MRI, where view shared k-space data is processed using Few-Shot MRI (FS-MRI) to improve reconstruction quality.

III. EXPERIMENTS

Our code will soon be available at <https://github.com/Silpa1>. The algorithm parameters for FS-MRI were initially tuned using single-coil speech, cardiac, brain, and PINCAT datasets, which were retrospectively sampled in a pseudo-radial manner. It was then evaluated on their multicoil versions, as well as on many other retrospective and prospective datasets sampled using many different sampling patterns – radial, spiral, Cartesian, and pseudo-radial. We employ pseudo-radial sampling to simulate two distinct under-sampling scenarios: (a) 3D Cartesian under-sampling, where phase encoding in the ky - kz

plane follows a radial ordering pattern [26], [27]; and (b) true 2D radial under-sampling, in which radial samples are pre-interpolated onto a Cartesian grid using a gridding approach such as GROG [28] prior to iterative reconstruction.

A. 17 Retrospectively Undersampled Datasets

The error value that we report in this and later sections is the normalized scale-invariant mean squared error (N-S-MSE), computed as follows: $Error = (\sum_{k=1}^q \text{dist}^2(x_k^*, \hat{x}_k)) / \|X^*\|_F^2$, where $\text{dist}^2(x^*, \hat{x}) = \|\hat{x} \frac{x^*}{\|x^*\|} - x^*\|_2^2$ is the scale-invariant distance between two vectorized images, where “scale” is a complex number. The reconstructed images can be complex-valued. The reporting format is **Error (Reconstruction Time in seconds)**. Although FS-MRI provides real-time reconstruction after α frames, we report the time required to reconstruct the entire MRI sequence to ensure a fair comparison with other methods.

We used a total of 17 datasets: 15 datasets across five different applications, that were retrospectively pseudo-radially undersampled with 4, 8 and 16 radial lines – brain-T2-T1-rho (Brain), free-breathing ungated cardiac perfusion (UnCardPerf), a long but low-resolution speech sequence (Speech), two cardiac cine datasets from the OCMR database (CardOCMR16, CardOCMR19) [29]. Additionally, we included 2 prospectively undersampled datasets from [6], where Cartesian variable density random undersampling was applied with reduction factors (R); R=8 for cardiac perfusion R8 (CardPerf-R8) and R=6 for cardiac cine R6 (CardCine-R6). Since fully sampled images were unavailable for these two prospectively sampled datasets, we used the converged reconstructions from [6] as reference images for error computation and visual comparisons. All datasets were multi-coil. Image sequence sizes: CardPerf-R8 ($n_x = 128, n_y = 128, q = 40$), CardCine-R6 ($n_x = 256, n_y = 256, q = 24$), Brain ($n_x = 128, n_y = 128, q = 24$), CardOCMR16 ($n_x = 192, n_y = 150, q = 15$), CardOCMR19 ($n_x = 192, n_y = 144, q = 25$), UnCardPerf ($n_x = 288, n_y = 108, q = 200$) and Speech ($n_x = 68, n_y = 68, q = 2048$).

In Table IIa, FS-MRI (proposed) is compared with real-time reconstruction techniques such as keyhole imaging [30], view-sharing [15], and OnAIR [17], as well as batch methods including L+S-Lin [6], L+S-Otazo [5], and zero-filled reconstruction. The last row reports the Average Error (Average Reconstruction Time), computed as the mean over the 17 previous rows. Keyhole imaging samples the low spatial frequencies (center of k-space) for each frame while reusing the high-frequency components (outer k-space) from a fully sampled reference frame, assuming that most temporal variations occur in the low-frequency region. To ensure a fair comparison, the number of center k-space samples per frame in keyhole imaging matches that used in FS-MRI. View-sharing [15] enhances temporal resolution in dynamic imaging by integrating phase-encoding lines from multiple frames. Repeated phase-encoding locations are averaged based on their frequency to ensure reconstruction consistency.

Since the authors’ implementations of keyhole imaging and view-sharing were unavailable, we implemented these

Dataset(Radial)	FS-MRI (proposed) Real-Time Delayed	KeyHole Imaging [30]	View Sharing [15]	OnAIR [17]	Zero-filled	L+S-Lin [6]	L+S-Otazo [5]
CardPerf-R8(0)	0.0201 0.0201 (12.10)	0.0230 (0.36)	0.0843 (1.02)	0.7460 (577.90)	0.3077 (0.19)	0.0292 (5.82)	0.0110 (18.23)
CardCine-R6(0)	0.0058 0.0058 (38.39)	0.0073 (0.80)	0.0318 (1.72)	0.5913 (837.17)	0.1734 (0.44)	0.0069 (16.40)	0.0054 (26.99)
Brain(4)	0.0125 0.0125 (4.29)	0.0314 (0.14)	0.0230 (0.28)	0.3242 (110.84)	0.2079 (0.07)	0.0173 (2.67)	0.0167 (6.22)
Brain(8)	0.0054 0.0054 (4.50)	0.0194 (0.14)	0.0216 (0.40)	0.1095 (103.39)	0.0901 (0.06)	0.0095 (2.62)	0.0086 (4.70)
Brain(16)	0.0027 0.0027 (4.19)	0.0115 (0.13)	0.0125 (0.39)	0.0731 (106.41)	0.0521 (0.07)	0.0062 (2.77)	0.0049 (3.22)
CardOCMR16(4)	0.0092 0.0092 (11.55)	0.0035 (0.13)	0.4068 (0.03)	0.9518 (218.38)	0.5344 (0.08)	0.0515 (3.36)	0.0293 (11.89)
CardOCMR16(8)	0.0033 0.0033 (7.96)	0.0029 (0.14)	0.3127 (0.17)	0.8972 (228.45)	0.3791 (0.08)	0.0101 (3.40)	0.0064 (10.31)
CardOCMR16(16)	0.0015 0.0015 (6.13)	0.0023 (0.16)	0.1780 (0.29)	0.8516 (240.93)	0.2208 (0.08)	0.0030 (2.90)	0.0035 (5.29)
CardOCMR19(4)	0.0095 0.0095 (11.97)	0.0099 (0.23)	0.4696 (0.32)	0.9465 (544.11)	0.5517 (0.15)	0.0698 (4.82)	0.0251 (19.60)
CardOCMR19(8)	0.0051 0.0051 (10.51)	0.0076 (0.22)	0.3421 (0.55)	0.8713 (511.15)	0.3815 (0.12)	0.0149 (5.47)	0.0092 (14.05)
CardOCMR19(16)	0.0032 0.0032 (9.11)	0.0056 (0.23)	0.1851 (0.57)	0.7875 (527.56)	0.2144 (0.13)	0.0044 (4.85)	0.0052 (7.41)
UnCardPerf(4)	0.0831 0.0790 (111.67)	0.2473 (2.06)	0.5630 (17.73)	0.9540 (6787.18)	0.5529 (1.25)	0.1424 (48.76)	0.0910 (194.09)
UnCardPerf(8)	0.0508 0.0482 (74.32)	0.1991 (2.04)	0.5000 (16.86)	0.8371 (4767.40)	0.4108 (1.36)	0.0632 (48.23)	0.0591 (122.56)
UnCardPerf(16)	0.0316 0.0295 (72.42)	0.1568 (2.07)	0.3315 (16.28)	0.6011 (4725.84)	0.2651 (1.29)	0.0329 (48.11)	0.0370 (89.47)
Speech(4)	0.1391 0.1326 (108.54)	0.4939 (3.71)	0.4107 (202.23)	0.7727 (28233.29)	0.4329 (2.02)	0.2545 (285.88)	0.1991 (524.47)
Speech(8)	0.0992 0.0930 (112.22)	0.3981 (3.59)	0.3229 (203.35)	0.5883 (25643.50)	0.3051 (2.06)	0.1284 (287.94)	0.1107 (482.62)
Speech(16)	0.0619 0.0584 (148.63)	0.3151 (3.59)	0.2162 (204.68)	0.4881 (28653.84)	0.1900 (2.06)	0.0557 (288.42)	0.0550 (414.29)
av-Err (av-Time)	0.0320 0.0305 (44.03)	0.1138 (1.16)	0.2595 (39.23)	0.6701 (6048.10)	0.3100 (0.6771)	0.0529 (62.49)	0.0398 (115.02)
av-Time per Frame	0.1069	0.0028	0.0953	14.6882	0.0016	0.1518	0.2793

(a) Errors and reconstruction times were obtained from MATLAB implementations.

Dataset(Radial)	FS-MRI (proposed) Real-Time Delayed	varMRI [9]	DEBLUR [10] using AGM-MRI	DEBLUR [10] using zero-filled as input	CineVN [8]
CardPerf-R8	0.0148 0.0148 (1.60)	0.2821 (9.25)	1.0000 (94.01)	1.0000 (94.16)	2.8680 (14.70)
CardCine-R6	0.0050 0.0050 (1.78)	0.0835 (13.83)	0.1054 (98.32)	0.1015 (98.80)	1.2105 (35.51)
Brain (4)	0.0126 0.0126 (3.46)	0.1170 (4.15)	0.2290 (91.87)	0.3158 (93.74)	1.2392 (6.71)
Brain (8)	0.0055 0.0055 (3.82)	0.0995 (4.53)	0.0569 (92.11)	0.1020 (92.08)	0.7326 (4.14)
Brain (16)	0.0027 0.0027 (3.75)	0.0754 (5.50)	0.0367 (92.18)	0.0330 (93.08)	0.4109 (4.74)
CardOCMR16 (4)	0.0093 0.0093 (2.41)	0.4837 (4.65)	0.3169 (93.93)	0.2928 (94.22)	1.1458 (11.41)
CardOCMR16 (8)	0.0034 0.0034 (1.48)	0.3932 (6.04)	0.1755 (94.30)	0.1937 (93.90)	1.0943 (5.28)
CardOCMR16 (16)	0.0015 0.0015 (0.92)	0.2160 (6.20)	0.1290 (93.97)	0.1294 (94.10)	1.0574 (4.49)
CardOCMR19 (4)	0.0097 0.0097 (13.85)	0.1786 (8.64)	0.6358 (92.92)	0.4991 (93.70)	2.4100 (13.14)
CardOCMR19 (8)	0.0051 0.0051 (11.21)	0.2101 (5.94)	0.7716 (93.33)	0.5931 (93.25)	2.6118 (11.59)
CardOCMR19 (16)	0.0032 0.0032 (9.11)	0.1734 (6.80)	0.3324 (93.00)	0.1897 (92.99)	1.4145 (11.72)
UnCardPerf (4)	0.0822 0.0867 (10.86)	0.0733 (66.61)	1.0000 (126.73)	0.9434 (127.61)	1.1797 (121.47)
UnCardPerf (8)	0.0517 0.0492 (9.75)	0.0639 (71.95)	0.7336 (119.74)	0.7004 (121.02)	1.1770 (131.32)
UnCardPerf (16)	0.0318 0.0295 (9.06)	0.0531 (77.38)	0.4719 (115.45)	0.6464 (114.94)	1.2272 (135.52)
Speech (4)	0.1393 0.1325 (66.74)	0.7990 (746.21)	1.0000 (382.56)	0.8296 (383.01)	2.1777 (247.22)
Speech (8)	0.0991 0.0934 (63.11)	0.7513 (746.30)	0.5312 (382.52)	0.5634 (383.16)	1.9687 (230.99)
Speech (16)	0.0621 0.0587 (56.91)	1.000 (745.47)	0.5755 (404.15)	0.4691 (404.38)	1.6928 (224.69)
av-Err (av-Time)	0.0317 0.0308 (15.87)	0.2972 (148.79)	0.4766 (150.65)	0.4472 (151.07)	1.5069 (71.45)
av-Time per Frame	0.0385	0.3613	0.3659	0.3669	0.1735

(b) Errors and reconstruction times were obtained from Python implementations on a GPU (A100).

TABLE II: The table format is **Error (Reconstruction time in seconds)**. The second-to-last row reports the average error and average reconstruction time (in seconds) over all 17 rows. The last row reports the average reconstruction time per frame (in seconds) computed by summing the time taken for processing all datasets and dividing by the total number of frames in all datasets. UnCardPerf stands for free-breathing ungated cardiac perfusion. In Table IIa, we compare FS-MRI (proposed) with the real-time methods and the LR methods. Due to lack of space, we did not show columns for k-tSLR [31] and altGDmin-mri [7]. K-tSLR average error was 0.0735 and average time was 1742.20. AltGDmin-MRI average error was 0.0308 and average time was 46.27. Table IIb compares FS-MRI (proposed) with DL-based batch methods.

methods in MATLAB. For OnAIR, L+S-Otazo, and L+S-Lin, we used the authors’ provided code: OnAIR: <https://github.com/JeffFessler/onair-lassi>, L+S-Lin: <https://github.com/JeffFessler/reproduce-l-s-dynamic-mri>, L+S-Otazo: <https://cai2r.net/resources/ls-reconstruction-matlab-code/>. The available OnAIR code is designed for video reconstruction; we modified it for MRI reconstruction. Our approach (FS-MRI) consistently achieves the best (low) error metrics among these methods.

Fig. 2 shows a single frame of the fully sampled image and its reconstructions using FS-MRI and other batch methods: AltGDmin-MRI [7] (slow-changing low-rank model), k-t-SLR [31] (low-rank and sparse model), and L+S-Otazo and L+S-Lin (low-rank plus sparse model) on the speech dataset. We used the authors’ provided code for all methods.

Figs. 3a and 3b show FS-MRI reconstructions in real-time and delayed settings, compared with keyhole imaging and view-sharing for the speech and UnCardPerf datasets, respectively. Keyhole imaging and view-sharing prioritize speed over accuracy. While they achieve faster reconstruction than FS-MRI, they often result in poor image quality, especially in the presence of significant inter-frame motion.

We compared FS-MRI with deep learning models, including unsupervised models such as DEBLUR [10] and VarMRI [9], as well as the supervised model CineVN [8], as shown in Table IIB. We used the author-provided code for all models: DEBLUR (author shared with us via email), VarMRI (<https://github.com/rushdi-rusho/varMRI>), and CineVN (<https://github.com/marcvornehm/CineVN>).

The VarMRI code requires the inverse Fourier transform of undersampled k-space data (zero-filled where data is absent) to be 168×168 for compatibility with the CNN architecture. To ensure this, we applied low-pass filtering, padding with zeros for smaller dimensions and cropping for larger ones. Without this preprocessing, dimension mismatches in the loss function cause errors. The VarMRI and DEBLUR codes were evaluated using non-Cartesian sampled data. We replaced the NUFFT operator with the FFT operator in the author’s code, which allows efficient processing of Cartesian sampled data. During training in VarMRI, the loss function $\sum_{k \in \mathcal{I}} \|\mathbf{A}_k^\top \mathbf{A}_k \mathbf{x}_k - \mathbf{A}_k^\top \mathbf{y}_k\|^2$ is used, where \mathcal{I} denotes the minibatch indices. This formulation accelerates training for non-Cartesian sampled data. For Cartesian sampled data, the standard loss function $\sum_{k \in \mathcal{I}} \|\mathbf{A}_k \mathbf{x}_k - \mathbf{y}_k\|^2$ is used, as suggested by the varMRI authors. DEBLUR uses two CNN-based generators trained on undersampled k-space data to learn spatial and temporal factors. However, in the provided implementation, spatial factors are updated using a CNN, while temporal factors are updated with a fully connected network (FCN), which differs from the original description in [10]. The DEBLUR code is initialized with STORM [32], but due to its unavailability, we used AltGDmin-MRI outputs for initialization. We also report results where DEBLUR is initialized with a zero-filled image (i.e., k-space data is zero-filled where data is unavailable). The provided code does not specify PyTorch versions, requiring updates for compatibility with newer packages. We tested CineVN on our datasets using the pretrained model parameters provided in the author’s code,

with an acceleration rate of 20. As shown in Table IIB, DL models performance was significantly worse, with a much longer inference time in the case supervised learning and reconstruction time for unsupervised and compared to FS-MRI.

However, as Table IIB shows, CineVN’s performance was noticeably worse. In comparison with FS-MRI, CineVN’s inference time was significantly longer. CineVN and other supervised learning techniques frequently don’t generalize to MRI applications that are different from their training data. In contrast to deep learning techniques, FS-MRI does not require application-specific parameter tuning and provides consistent performance across various applications. Visual comparisons are shown in Figs. 4a–4b. In Fig. 4a, we observe that VarMRI and CineVN fail completely, both returning black images. While DEBLUR captures some structural details, it completely fails to capture motion. For the brain dataset, while DEBLUR captures structural details, it fails to capture the contrast uptake, as shown in Fig. 4b. For both these datasets, FS-MRI provides reconstructions that are comparable to the fully sampled image.

B. 6 prospectively under-sampled datasets

We used a total of six prospectively undersampled datasets: four Cartesian undersampled cardiac datasets, a radially undersampled abdomen dataset, and a spirally undersampled speech dataset. Important thing to note that, keyhole Imaging method cannot be applied to these datasets, as they require fully sampled k-space data as a reference frame, which these prospectively sampled datasets do not satisfy.

Our first two datasets are Cartesian undersampled cardiac cine prospective datasets from the OCMR database. The first dataset has k-space dimensions of 384 readout points, 14 phase-encode lines per time frame, 137 time frames, and 18 coils, while the second dataset has k-space dimensions of 384 readout points, 16 phase-encode lines per time frame, 65 time frames, and 34 coils. As shown in Figs. 5a-5b, FS-MRI RT and FS-MRI Del reconstructions achieve high-quality results for both datasets, whereas view-sharing introduces motion blurring in both cases.

Our next two prospective datasets are CardPerf-R8 and CardCine-R6, as mentioned in Section III-A. Fig. 5c shows that FS-MRI provides good reconstructions for the CardCine-R6 dataset, while L+S-Lin reconstructions exhibit slight blurring in the temporal domain. As shown in Fig. 5d, both FS-MRI and L+S-Lin provides high-quality images for CardPerf-R8 dataset.

Our last two prospective datasets are non-Cartesian sampled. The first dataset is a radially undersampled dynamic contrast-enhanced (DCE) abdomen dataset from [6]. The second dataset is a spirally undersampled speech dataset from [33]. To handle non-Cartesian sampling, we incorporate the non-uniform Fast Fourier Transform (NUFFT) function from [6] instead of the standard FFT and include density compensation. The k-space data for the DCE abdomen dataset consists of 384 readout points, 21 radial spokes per frame (with golden-angle-based angular increments), 28 time frames, and 7 virtual coils after PCA-based coil compression. The 21 spokes per frame result

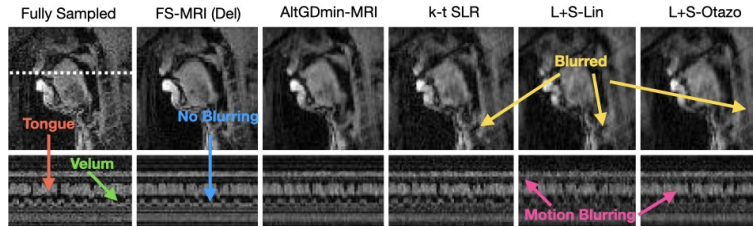
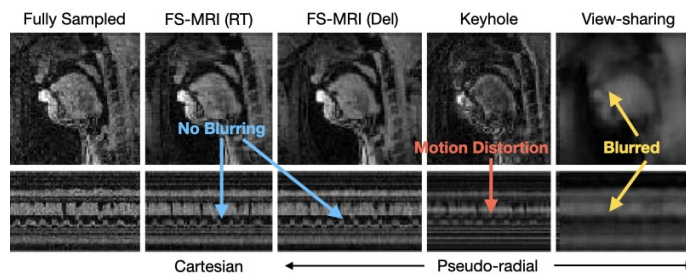
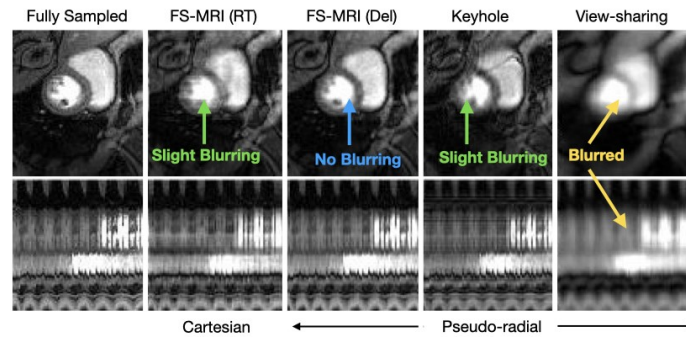


Fig. 2: Retrospective, Pseudo-radial (4 radial lines), Speech: The first row shows the 1470-th frame of the fully sampled image and its reconstructions using FS-MRI and with batch methods. The second row shows the time profile image to illustrate the motion of the tongue and velum. For simplicity, we display a cut through 100 frames, as indicated in the original frame. Error (Reconstruction time in seconds): FS-MRI: 0.1326 (108.54), AltGDmin-MRI: 0.1416 (114.37), k-t SLR: 0.1543 (5189.96), L+S-Lin: 0.2545 (285.88) and L+S-Otazo: 0.1991 (524.47). Error (Reconstruction time in seconds) for 16 radial lines: FS-MRI: 0.0584 (148.63), AltGDmin-MRI: 0.0580 (209.56).

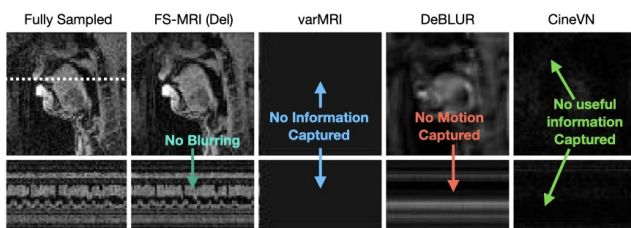


(a) Speech, Pseudo-radial (4 radial lines) and Cartesian ($R = 6$)

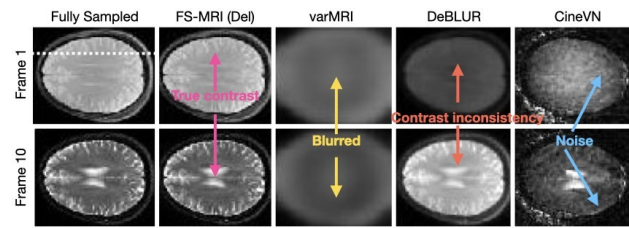


(b) Free-breathing ungated cardiac perfusion (UnCardPerf), Pseudo-radial (16 radial lines) and Cartesian ($R = 6$)

Fig. 3: Retrospective: Both figures show fully sampled images and their reconstructions using FS-MRI (proposed) and real-time methods. Row 1 of Fig. 3a and Fig. 3b shows the 2000-th and 76-th frames, respectively, while Row 2 shows the corresponding time profiles. Cartesian sampling uses variable-density random undersampling.



(a) Speech



(b) Brain

Fig. 4: Retrospective, Pseudo-radial (16 radial lines): Fig. 4a and Fig. 4b show fully sampled images and their reconstructions using FS-MRI (proposed) and batch DL methods—VarMRI [9], DEBLUR [10], and CineVN [8]—for the speech and brain datasets, respectively. In first row of Fig. 4a, we show the 1470-th frame, while row 2 shows the time profile images. In first and second row of Fig. 4b, we show the 1-st and 10-th frames, respectively.

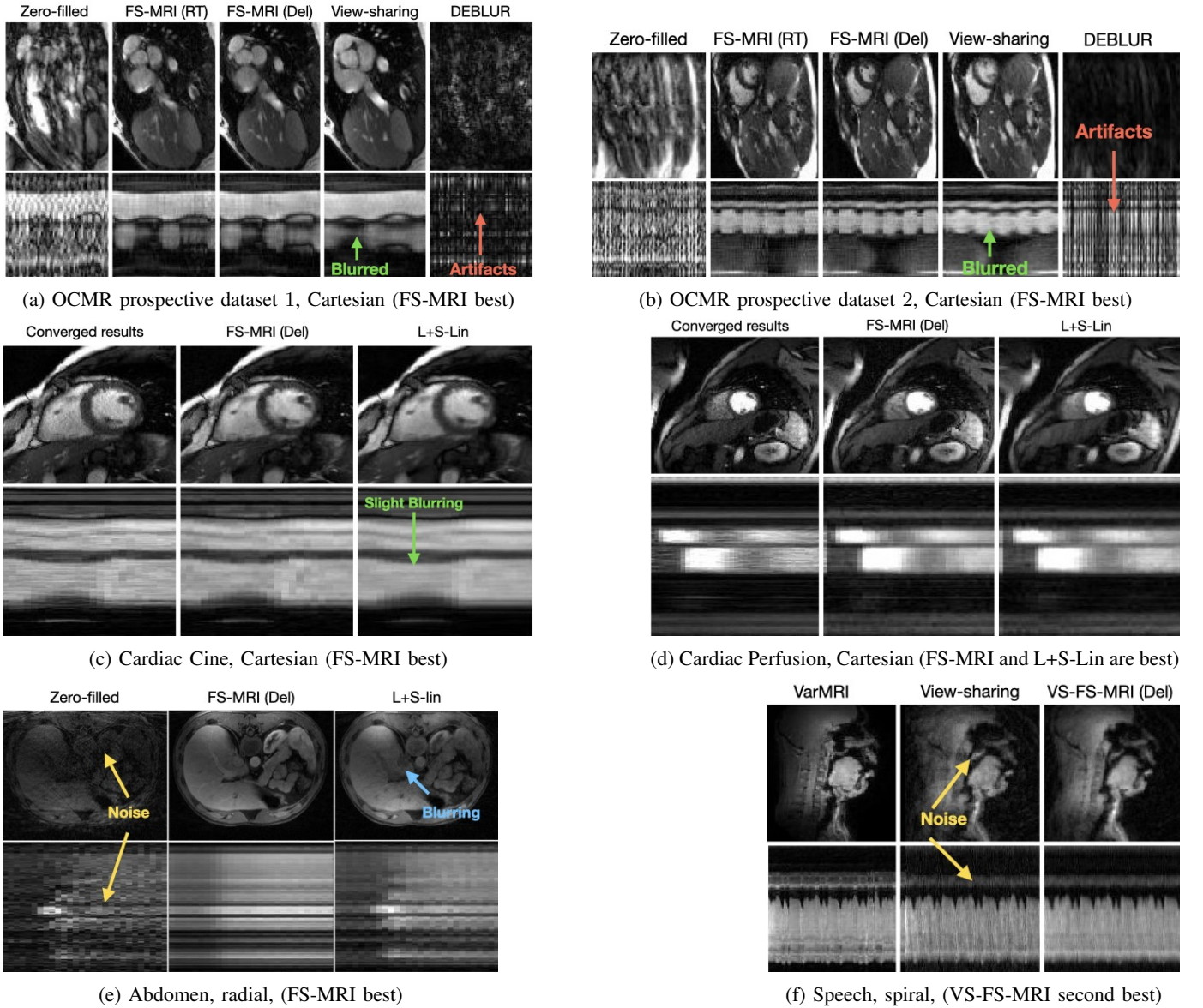


Fig. 5: Prospective: Fig. 5a - 5e show reconstructions of different MRI applications using FS-MRI and other methods in Row 1, while Row 2 shows the corresponding time profile images. In Fig. 5a - 5b, we compare FS-MRI (both real-time and delayed) with zero-filled, view-sharing, and DEBLUR. In Fig. 5c and Fig. 5d, we compare FS-MRI with converged results from [6] and L+S-Lin. In Fig. 5e, we compare FS-MRI (Real-Time) reconstructions with zero-filled and L+S-Lin. This dataset was used in [6]. In Fig. 5f, we compare reconstructions from varMRI, view-sharing, and VS-FS-MRI. VarMRI produces better image quality as it is specifically designed for this dataset. VS-FS-MRI reduces noise in view-sharing reconstructions.

in a total of 588 spokes (21×28), which are distributed across 28 time frames such that each frame is formed by a set of 21 consecutive spokes. As shown in Fig. 5e, FS-MRI and L+S-Lin reconstructions effectively capture contrast uptake dynamics in the liver. While FS-MRI clearly resolves other blood vessels, L+S-Lin exhibits slight blurring.

The spirally undersampled speech dataset consists of k-space data with 335 readout points per spiral interleaf, 3 interleaves per frame, 900 frames, 8 virtual coils, and 10 slices, with an image resolution of 168×168 . For simplicity, we focus on a single slice in our experiments. This dataset was originally designed for VarMRI with optimized parameters. We compare the performance of VarMRI, view-sharing, and FS-MRI. While VarMRI yields high-quality reconstructions, view-

sharing introduces noise in the reconstructed images. However, our proposed VS-FS-MRI method effectively reduces noise effect while preserving structural details, as shown in Fig. 5f.

IV. DISCUSSION AND CONCLUSIONS

This work introduces a new algorithm called Dynamic Few Shot MRI (FS-MRI) and its view-sharing extension, VS-FS-MRI, for fast near real-time and generalizable dynamic MRI. Improved quality delayed reconstructions are also provided. Here near real-time means the acquisition is quick, the algorithm is zero-latency after the first short mini-batch, and the reconstruction time taken per frame (average of 0.04 seconds) is less than the acquisition time per frame. Generalizable means the same algorithm without any parameter tuning works

for different MRI applications, sampling schemes and rates, making it practically usable on an MRI scanner. One reason for the fast speed of our algorithm is that it is also memory-efficient: it needs only order $\max(n, \alpha)r$ memory, where α is the mini-batch length and n is the number of pixels of a reconstructed image. For the same reason, and because there are no iterative sub-steps within the main algorithm iteration, it is also very efficient to distribute onto multiple cores (or for larger problems on the cloud) to speed-up further. The Python GPU implementation uses this fact.

1) *Limitations*: As observed in our results, the proposed reconstruction algorithm does not achieve the best performance across all applications. In some cases, such as UnCardPerf, blurring artifacts are noticeable when it is heavily undersampled. These artifacts can be mitigated by tuning parameters such as step size, maximum number of iterations, the rank of the low-rank component, and by designing more robust loop exit criterion. However, our goal is to show the performance of the algorithm using a single set of parameters. It is important to note that when the motion is large and the k-space data is heavily undersampled, the mean and LR components may fail to capture the full extent of the motion. In such cases, the last step of updating e_k is the one that needs to capture the motion. When it does not, artifacts appear. Maybe using more iterations or using a canonical sparse model on it may help.

REFERENCES

- [1] S. Babu, S. G. Lingala, and N. Vaswani, "Generalizable real-time accelerated dynamic mri," in *ICASSP 2025*.
- [2] M. Lustig, D. Donoho, and J. M. Pauly, "Sparse MRI: The application of compressed sensing for rapid mr imaging," *Magnetic Resonance in Medicine*, vol. 58(6), pp. 1182–1195, December 2007.
- [3] B. Zhao, J. P. Haldar, A. G. Christodoulou, and Z.-P. Liang, "Image reconstruction from highly undersampled-space data with joint partial separability and sparsity constraints," *Medical Imaging, IEEE Transactions on*, vol. 31, no. 9, pp. 1809–1820, 2012.
- [4] S. G. Lingala, Y. Hu, E. DiBella, and M. Jacob, "Accelerated dynamic mri exploiting sparsity and low-rank structure: kt slr," *Medical Imaging, IEEE Transactions on*, vol. 30, no. 5, pp. 1042–1054, 2011.
- [5] R. Otazo, E. Candes, and D. K. Sodickson, "Low-rank plus sparse matrix decomposition for accelerated dynamic mri with separation of background and dynamic components," *Magnetic resonance in medicine*, vol. 73, no. 3, pp. 1125–1136, 2015.
- [6] C. Y. Lin and J. A. Fessler, "Accelerated methods for low-rank plus sparse image reconstruction," in *2018 IEEE 15th International Symposium on Biomedical Imaging (ISBI 2018)*. IEEE, 2018, pp. 48–51.
- [7] S. Babu, S. G. Lingala, and N. Vaswani, "Fast low rank compressive sensing for accelerated dynamic MRI," *IEEE Trans. Comput. Imag.*, 2023.
- [8] M. Vornehm, J. Wetzl, D. Giese, F. Furnrohr, J. Pang, K. Chow, R. Gebker, R. Ahmad, and F. Knoll, "Cinevn: Variational network reconstruction for rapid functional cardiac cine mri," *Magnetic Resonance in Medicine*, vol. 93, no. 1, pp. 138–150, 2025.
- [9] R. Z. Rusho, Q. Zou, W. Alam, S. Erattakulanga, M. Jacob, and S. G. Lingala, "Accelerated pseudo 3d dynamic speech mr imaging at 3t using unsupervised deep variational manifold learning," in *MICCAI, 2022*.
- [10] A. H. Ahmed, Q. Zou, P. Nagpal, and M. Jacob, "Dynamic imaging using deep bi-linear unsupervised representation (deblur)," *IEEE Transactions on Medical Imaging*, vol. 41, no. 10, pp. 2693–2703, 2022.
- [11] M. Blumenthal, C. Fantinato, C. Unterberg-Buchwald, M. Haltmeier, X. Wang, and M. Uecker, "Self-supervised learning for improved calibrationless radial mri with nlinv-net," *Magnetic Resonance in Medicine*, vol. 92, no. 6, pp. 2447–2463, 2024.
- [12] A. Majumdar, R. K. Ward, and T. Aboulnasr, "Compressed sensing based real-time dynamic mri reconstruction," *IEEE Transactions on Medical Imaging*, vol. 31, no. 12, pp. 2253–2266, 2012.
- [13] M. Uecker, S. Zhang, and J. Frahm, "Nonlinear inverse reconstruction for real-time mri of the human heart using undersampled radial flash," *Magnetic Resonance in Medicine*, vol. 63, no. 6, pp. 1456–1462, 2010.
- [14] M. Uecker, S. Zhang, D. Voit, A. Karaus, K.-D. Merboldt, and J. Frahm, "Real-time mri at a resolution of 20 ms," *NMR in Biomedicine*, vol. 23, no. 8, pp. 986–994.
- [15] S. Narayanan, K. Nayak, S. Lee, A. Sethy, and D. Byrd, "An approach to real-time magnetic resonance imaging for speech production," *The Journal of the Acoustical Society of America*, vol. 115, no. 4, pp. 1771–1776, 2004.
- [16] S. Ravishankar, B. E. Moore, R. R. Nadakuditi, and J. A. Fessler, "Low-rank and adaptive sparse signal (lassi) models for highly accelerated dynamic imaging," *IEEE Transactions on Medical Imaging*, vol. 36, no. 5, pp. 1116–1128, 2017.
- [17] B. E. Moore, S. Ravishankar, R. R. Nadakuditi, and J. A. Fessler, "Online adaptive image reconstruction (onair) using dictionary models," *IEEE transactions on computational imaging*, vol. 6, pp. 153–166, 2019.
- [18] K. S. Nayak, Y. Lim, A. E. Campbell-Washburn, and J. Steeden, "Real-time magnetic resonance imaging," *Journal of Magnetic Resonance Imaging*, vol. 55, no. 1, pp. 81–99, 2022.
- [19] S. S. Du, W. Hu, S. M. Kakade, J. D. Lee, and Q. Lei, "Few-shot learning via learning the representation, provably," in *Intl. Conf. Learning Representations (ICLR)*, 2021.
- [20] K. K. Thekumparampil, P. Jain, P. Netrapalli, and S. Oh, "Statistically and computationally efficient linear meta-representation learning," *Advances in Neural Information Processing Systems*, vol. 34, pp. 18487–18500, 2021.
- [21] A. P. Singh and N. Vaswani, "Byzantine resilient and fast federated few-shot learning," in *International Conference on Machine Learning (ICML)*, 2024.
- [22] F. Alshehri and G. Muhammad, "A few-shot learning-based ischemic stroke segmentation system using weighted mri fusion," *Image and Vision Computing*, vol. 140, p. 104865, 2023.
- [23] J. A. Fessler and B. P. Sutton, "Nonuniform fast fourier transforms using min-max interpolation," *IEEE Transactions on Signal Processing*, vol. 51, no. 2, pp. 560–574, 2003.
- [24] S. Nayer and N. Vaswani, "Fast and sample-efficient federated low rank matrix recovery from column-wise linear and quadratic projections," *IEEE Trans. Info. Th.*, Feb. 2023, arXiv:2102.10217 (Feb. 2021).
- [25] S. Babu, S. Nayer, S. G. Lingala, and N. Vaswani, "Fast low rank compressive sensing for accelerated dynamic mri," in *IEEE Intl. Conf. Acoustics, Speech, Sig. Proc. (ICASSP)*, 2022.
- [26] J. Y. Cheng, T. Zhang, N. Ruangwattanapaisarn, M. T. Alley, M. Uecker, J. M. Pauly, M. Lustig, and S. S. Vasanawala, "Free-breathing pediatric mri with nonrigid motion correction and acceleration," *Journal of Magnetic Resonance Imaging*, vol. 42, no. 2, pp. 407–420, 2015.
- [27] F. Han, Z. Zhou, M. Cao, Y. Yang, K. Sheng, and P. Hu, "Respiratory motion-resolved, self-gated 4d-mri using rotating cartesian k-space (rock)," *Medical physics*, vol. 44, no. 4, pp. 1359–1368, 2017.
- [28] T. Benkert, Y. Tian, C. Huang, E. V. DiBella, H. Chandarana, and L. Feng, "Optimization and validation of accelerated golden-angle radial sparse mri reconstruction with self-calibrating grappa operator gridding," *Magnetic resonance in medicine*, vol. 80, no. 1, pp. 286–293, 2018.
- [29] C. Chen, Y. Liu, P. Schniter, M. Tong, K. Zareba, O. Simonetti, L. Potter, and R. Ahmad, "Ocmr (v1. 0)–open-access multi-coil k-space dataset for cardiovascular magnetic resonance imaging," *arXiv preprint arXiv:2008.03410*, 2020.
- [30] J. L. Duerk, J. S. Lewin, and D. H. Wu, "Application of keyhole imaging to interventional mri: a simulation study to predict sequence requirements," *Journal of Magnetic Resonance Imaging*, vol. 6, no. 6, pp. 918–924, 1996.
- [31] S. G. Lingala, E. DiBella, G. Adluru, C. McGann, and M. Jacob, "Accelerating free breathing myocardial perfusion mri using multi coil radial k-t slr," *Physics in medicine and biology*, vol. 58, no. 20, p. 7309, 2013.
- [32] S. Poddar and M. Jacob, "Dynamic mri using smoothness regularization on manifolds (storm)," *IEEE transactions on medical imaging*, vol. 35, no. 4, pp. 1106–1115, 2015.
- [33] R. Z. Rusho, "Speech MRI dataset of repeated counting from 1-5," 9 2022. [Online]. Available: https://figshare.com/articles/dataset/Speech_MRI_dataset_of_repeated_counting_from_1-5/20468559